JrnlID 170_ArtID 7184_Proof# 1 - 09/05/2021

The International Journal of Advanced Manufacturing Technology
https://doi.org/10.1007/s00170-021-07184-2

ORIGINAL ARTICLE

Friction stir welding of AA2024-T3: development of numerical simulation considering thermal history and heat generation

Cyrus Amini[1] · Soran Hasanifard[1] · Mohammad Zehsaz[1] · Ramon Jerez-Mesa[2] · J. Antonio Travieso-Rodriguez[2]

Received: 4 November 2020 / Accepted: 29 April 2021

Abstract
This paper proposes a finite element model implemented in ANSYS using Lagrangian formulation to assess heat generation and friction dynamics of a friction stir welding process on AA2024-T3 aluminum plates. For that aim, the model is enriched by estimating a temperature-dependent friction coefficient using theoretical relationships, and by considering a temperature-dependent multilinear isotropic hardening equation as a plasticity model representing the material. Both quantitative determinations are confirmed through experimental data collected on the real material. Finally, the contact conditions are modeled using the modified Coulomb criterion. The results of the model are in agreement with actual results observed on experimental applications. The study proves that the rotational speed of the tool is the most determinant factor in the results. As it rises, the friction-generated heat flow is higher. This study shows that the compressive stress-strain data in strain rate of $10s^{-1}$ is a good approximation of the plasticity behavior of aluminum alloy during the friction stir welding.

Keywords Temperature-dependent friction · Friction stir welding · Frictional heat generated

1 Introduction

As a novel solid-state joining technique, friction stir welding (FSW) has earned great interest for many researchers during the last years. Indeed, the weld seam produced by FSW is free of many defections which are common in fusion welding for aluminum alloys, like hot cracking (HC) or stress corrosion cracking (SCC). Furthermore, the low residual stress present in the material after applying this method, compared with other welding processes has led it into wide acceptance in the fabrication of structures requiring high strength-to-weight ratio [1, 2].

✉ Cyrus Amini
camini@tabrizu.ac.ir

[1] Mechanical Engineering Department, University of Tabriz, 29 Bahman Blvd, Tabriz 5166616471, Iran

[2] Escola d'Enginyeria de Barcelona Est, Mechanical Engineering Department, Universitat Politècnica de Catalunya, Carrer d'Eduard Maristany, 10-12. 08019, Barcelona, Spain

During the first stage of FSW, a rotating tool slowly plunges into the contact surface of two plates which are firmly clamped on the milling machine's vice until the shoulder of the tool touches the upper surfaces of both plates and the generated heat softens the materials. During the second phase, the rotating tool moves along the plates with traverse speed (Fig. 1). While moving, the tool forges the materials by creating a permanent joint [3]. Of course, the scope of application of FSW in terms of testing on various materials [4–8] and implementation routines [9, 10] is changing and improving.

Since the invention of FSW, several researchers have performed many studies to understand the characteristics of material's flow around the welding tool, to estimate heat generation and heat loss, and to interpret microstructural observations. Some of them have succeeded in tackling with the mentioned issues by applying specific simplifications. However, because of the many variables involved in this process, the information obtained from experimental tests is very limited, and a lot of welding tests are needed to fully understand the process itself [11]. Due to time consumption and other disadvantages, the necessity of introducing a comprehensive numerical model covering the effective temperature-dependent properties and contact states in the FSW process, has motivated the development of the works included in this paper.

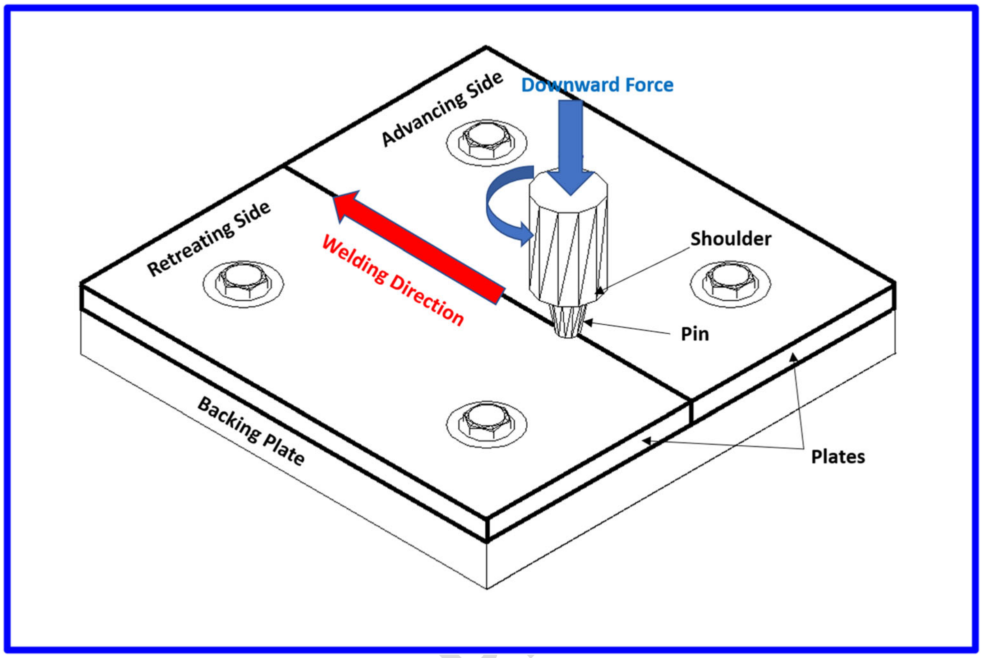

Fig. 1 Display of FSW process

In FSW, the temperature distribution inside the workpiece is of utter importance, as it affects the thermal stress during and after the process. The stress and strain fields are originated in thermal and mechanical stresses exerted to the joint during the welding process and are responsible for the residual stress and the displacement fields, that can eventually result in the final distortion of the weld joint [12]. That is why many researchers have been working on the modeling of heat transfer during FSW to estimate the heat and temperature distributions. The challenge in tackling this issue is managing the high number of parameters implicated in the process.

The main sources of heat generation during FSW are dual. The first one is the friction between tool and plates. Secondly, the heat that is generated by plastic deformation. For that reason, some researchers have tried to utilize a moving heat source to obtain final temperature distributions, by decoupling both phenomena [13, 14]. But because the mechanism implicated in FSW are fully coupled, i.e., the energy generation is related to material flow and contact condition and vice versa [15], a thorough simulation should include material flow and state condition in direct couple analysis.

On the other hand, the contact condition between the tool and workpiece is described by two parameters, namely the frictional coefficient and slip rate. In previous research works, some models of heat generation just considered the sliding friction assuming constant friction coefficient and therefore neglecting the influence of material flow [16–19]. Colegrove and Shercliff suggested 2-D axisymmetric model and considered sticking over a reduced radius below the shoulder to represent slipping near the shoulder periphery by assuming constant friction coefficient [20, 21]. Ulysse [22] only considered plastic deformation as the unique heat source, i.e., a full sticking condition was assumed. Heurtier et al. [23] considered two heat generation ways form, namely sliding or sticking, but the authors developed an uncoupled model because modeling the combination of these sources is complex. In the meantime, some experts utilized an Arbitrary Lagrangian Eulerian (ALE) approach at local scale to model the plastic deformation [24] and thermal analysis [25] at a constant Young's modulus, conductivity and special capacity. A good correlation was found with the real experimental results, although this approach did not cover the interactions at the contact surface comprehensively (for example, they did not consider the maximum temperature-dependent shear stress at the contact surface). Meyghani et al [26] applied a temperature-dependent Young's module to improve the accuracy of result at stirring zone using the ALE approach.

Most simulations in the literature considered the Johnson-Cook (JC) model or elastic-viscoelastic model as plasticity model in aluminum alloys. Some researchers [20, 21] used the equation was proposed and modified by Sheppard and Wright to describe the flow strength of aluminum alloy which overestimated flow stress compared to the experimental data. However, many researchers have shown that these models, especially the JC model, deviate from the actual plastic behavior at high temperatures. For that reason, further research led to introduce in the model more accurate constitutive equations [27–30]. At sight of the variety of modified constitutive models used previously, it seems that applying a temperature-dependent plastic model based on experimental data is more reasonable.

As it was mentioned above, the main source of heat generation is derived from friction between tool and plates. That is why one of the most challenging issues in FSW is the estimation of friction as a function of temperature. Many authors suggested a constant friction coefficient within the range of 0.3–0.5 [15–17]. Mijajlovic et al. [31] introduced a relation based on tangential and axial forces (from experimental work) for the estimation of constant friction coefficient. Su et al. [28] proposed an improved method simultaneously slip rate and friction coefficient. Meyghani et al. [32] also developed a finite element model (FEM) by calculating the temperature-dependent friction coefficient, assuming that the shear stress ratio between the shoulder and pin side is constant within the process.

In this study, a three-dimensional model is proposed to overcome the main drawbacks of past models presented above, in order to investigate the temperature distribution and heat generation dynamics. More specifically, it presents the following characteristics:

1. Applying a temperature-dependent multilinear isotropic hardening model in direct couple analysis, which includes yield Stress, the Young's Modulus and flow stress varying with temperature based on experimental data to improve plastic behavior.
2. Utilizing a temperature-dependent frictional coefficient considering a variable ratio of shear stress at the shoulder to the pin. In calculating this parameter, the effect of the slip rate is taken into account. Temperature-dependent friction coefficients were estimated at any rotational speed.
3. Using the Lagrangian approach to investigate FSW, which is free of subsequent remeshing (compared with ALE resulting temperature gap at the stirring zone) within the process. This approach makes possible to describe complicate interactions at the contact surfaces and investigate the tool and workpiece of FSW at the global level.

The combination of the three previous descriptors constitutes the main novelty introduced by this investigation and the works presented in this paper. Developing a successful FSW model is of utter importance for strategic manufacturing sectors where the optimization of process parameters constitutes the main driver of excellence.

2 Materials and experimental methods

2.1 Experimentation

The improved method to estimate the friction coefficient between the FSW tool and the material requires input parameters such as axial load and torque. For that reason, experimental tests were conducted to record these parameters during the process, considering the effect of two main process descriptors: rotational speed and tool traverse speed (welding speed). The recording of these parameters during actual Table 1 represents the testing conditions performed to estimate the friction coefficient. They were planned by following a 2-level factorial experimental design with two variables with a center point was used to guide the experiment method, as shown in Table 1. It allowed us to define a special parameter named weld pitch, that is, the ratio of the tool traverse speed to the rotational speed. Using this parameter, the influence of each speed would be investigated independently.

The experimental outline is shown in Fig. 1. The plates were fabricated in AA2024-T3 aluminum alloy of 3 mm thickness, 80 mm width and 100 mm length. A tool with taper pin was used. The height of the pin is 2.7 mm and the pin diameter at the top and the tip are 5.5 mm and 4.5 mm respectively. The diameter of shoulder was 14 mm. The tool was made up of Tungsten carbide with:

$$\text{Density}, \rho = 15000\,\frac{Kg}{m^3},\ \text{Young's Modulus}, E = 630\ GPa,$$
$$\text{Coductivity}, k = 85\,\frac{W}{mK},\ \ \text{Poisson ratio}, \upsilon = 0.24,$$
$$\text{and Specific heat}, C = 280\,\frac{J}{kg.K}$$

The experiments were conducted in a milling machine LAGUN MC600 with maximum power of 5 kW. The forces experimented by the samples derived from the process were measured with a dynamometric table of forces Kistler type 9129AA. For data acquisition, a multichannel charge amplifier type Kistler 5070 and DynoWare type 5697A were used. The sampling rate was set to 50 Hz. Since the torque measured by the system changes as the tool moves transversely due to the fact that the relative distance to the sensors changed accordingly, a MATLAB script was programmed to recalculate the real torque M, for each position of the tool (Eq. (1))

$$M(t^{\times}) = \left(f_{x4+3} - f_{x1+2}\right)b + \left(f_{y4+1} - f_{y3+2}\right)vt^{\times} + \left(0.012 * f_{y4+1}\right) - \left(0.054 * f_{y3+2}\right) \quad (1)$$

where $t^{\times}$ is difference between time and start time, v is welding speed, f_i is output from corresponding channel, and b is a geometrical parameter of the dynamometric table (half of

Table 1 Experimental design during FSW

Test	Rotational speed (min^{-1})	Welding speed (mm/min)
1	550	20
2	550	40
3	825	30
4	1100	20
5	1100	40

Table 2 Chemical composition of workpiece AA2024-T3

Element	Si	Fe	Cu	Mn	Mg	Cr	Zn	Ti	Al
Weight%	0.13	0.5	4.8	0.72	1.41	0.1	0.07	0.15	balanced

lateral distance of two parallel channel) equal to 50.5 mm (Table 2).

Measuring the temperature at certain points has been used as a verification between the FEM model and experimental results. With that aim, six K-type thermocouples along with a Pico data logger type TC-08 were applied in which sampling rate was set to 60 Hz. The Fluke 62 MAX IR thermometer is used for measuring temperature near the tool (Fig. 2).

2.2 Temperature-dependent plasticity model

Common constitutive equations for flow stress in friction stir welding are function of strain and strain rate and temperature, which are strain-independent at high temperatures. Studies showed that at the tool-workpiece interface, the temperature is located between 0.6Tm and 0.9Tm [33]. And the strain rate was estimated between 10 and 100s^{-1} by relating the grain size with the Zener-Hollomon parameters [34, 35]. On the other hand, some authors [36–38] claimed the range of strain rate during aluminum alloy FSW is lower than 10s^{-1}. In order to the study of plastic deformation behavior of friction stir welded aluminum alloy 2024 Zhang et al. considered stress-strain curve aluminum alloy in different strain rate level of 0.01 to 10s^{-1} [39].

The study of flow stress for hot deformation of Al2024-T3 shows that the range of flow stress for strain rate of 10 to 100s^{-1} at high temperature (more than 350° C) is not significantly different but these experimental data have some deviations from the stress predicted by the common models (like Johnson-Cook and Arrhenius-type) [30].

Using flow stress experimental data for Al2024-T3 [39] and compressive strain-stress curves for Al2024 alloy in different temperature and strain rate of 10s^{-1} [30] temperature-dependent compressive stress-strain curves for Al2024-T3 in strain rate of 10s^{-1} was derived (Fig. 3).

The adopted curves cover Young modulus (20-73.1GPa), elastic strain (0.001–0.0045) and yield stress (86-345MPa). In this study, a model is presented that satisfies both the experimental flow stress data during FSW process and fully covers the elastic behavior of the material. In this work, temperature-dependent multilinear isotropic hardening is used as plasticity model and uses stress-strain curves in Fig. 3. It is capable of simulating elastic, plastic, large strain, and large deformation [40].

In addition to the hardening rule (according to mentioned strain and stress curves), two distinct criteria have been used to determine this plasticity model: 1- flow rule 2- yield criterion. Flow rule determines the increment in plastic strain from the increment load. associative flow rule is used as follows:

Fig. 2 (**a**) Photograph and (b) schematic of plates, fixture, detective force, and thermocouples used in the FSW process

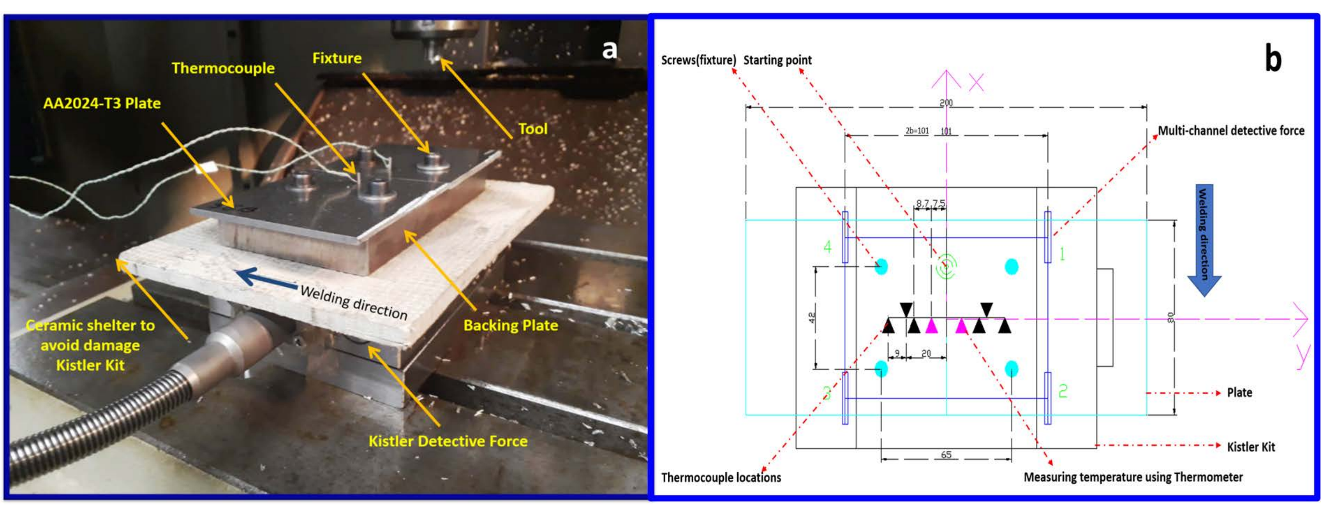

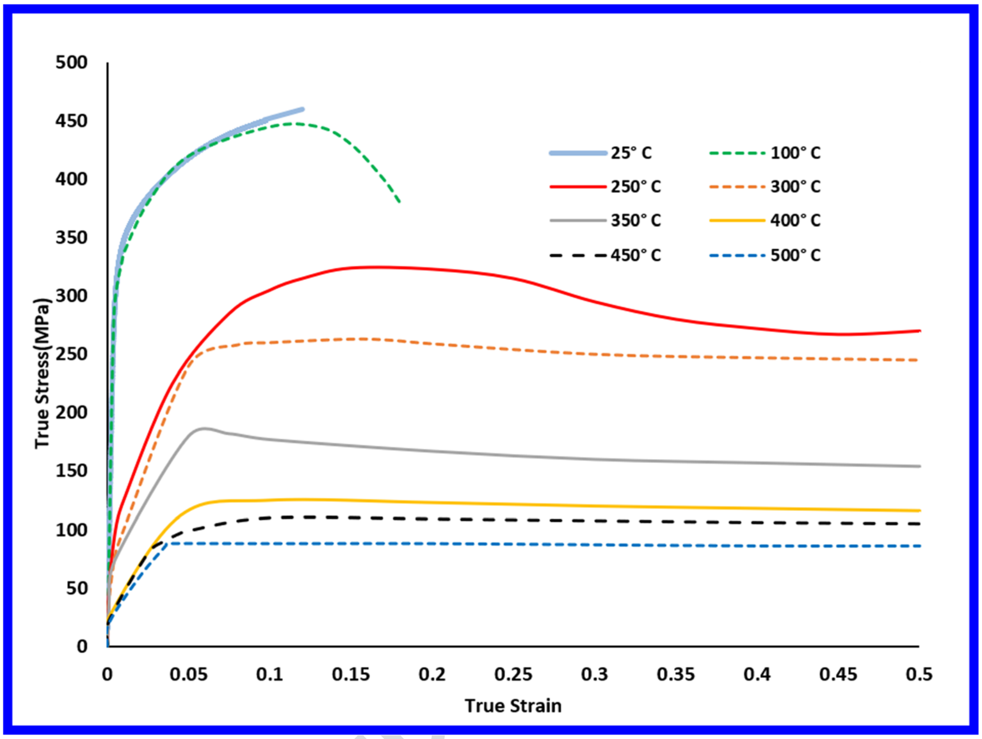

Fig. 3 True stress-strain diagram of the aluminum alloy at strain rate of $10s^{-1}$

$$\{d\varepsilon^p\} = d\lambda\left\{\frac{\partial G}{\partial \sigma}\right\} \tag{2}$$

where $d\varepsilon^p$ is increment in plastic strain, dλ is the magnitude of plastic stain increment, G is plastic potential and σ is stress. The Von misses yield criterion applied in this current study as a yield criterion as follows [41]:

$$f(\sigma_e - \sigma_y) = 0 \quad , \qquad \sigma_e = \sqrt{\frac{3}{2}\left(\sigma:\sigma - \frac{tr(\sigma)^2}{3}\right)} \tag{3}$$

Other thermo-physical and structural properties of aluminum alloy 2024-T3 used in the simulation are presented in Table 3.

2.3 Estimation of temperature-dependent friction coefficient

Determining the variation of the friction coefficient with the temperature is an ambiguous issue. Researchers have made efforts to overcome this challenge, by considering different strategies. For instance, taking a constant value of 0.3 for the steel-aluminum contact [15–17], making an approximation of a constant value based on an experimental relation [31], defining friction coefficient as a function of angular velocity and slip factor [46] or by making assumptions like considering a constant value of the axial pressure or of the shear stress ratio throughout the process to introduce a range of temperature-dependent friction coefficient [32].

In this study, an improved method, which is independent of the above assumptions and is based on empirical data and

Table 3 AA2024-T3 structural and thermo-physical properties [42–45]

Structural properties								
Density, ρ	2780 kg/m^3			*Poisson's ratio, υ*			0.33	
Thermo-physical properties								
Temp.	25°C	100°C		200°C	300°C		400°C	
k (W/mK)	121.8	134.9		151.2	172.2		176.4	
C (J/kg K)	921	921		1047	1130		1172	
α (10^{-6} K^{-1})	22.5	22.9		23.8	24.7		24.7	
Temp.	25 °C	100°C	149°C	190°C	260°C	316°C	371°C	400°C
E (GPa)	73.3	71	68.2	64.8	58	49.6	35.8	28

accepted theoretical relationships, is proposed to estimate temperature-dependent friction coefficient. It is based on considering the dimensionless variable named contact state variable δ, obtained by dividing the velocity of workpiece by the velocity of the FSW tool. When compared to the yield shear stress of the material at temperature T ($\tau_y(T)$), it defines the regime in the FSW [2].

During FSW, sliding and sticking appear simultaneously in the interface between the tool tip and the surface and δ is located between zero and one [2]. Given such a result, Sue et al. reached an analytical relationship to compute δ and μ friction coefficient as explained in Eq. (4) [29]:

$$\delta = \frac{S_1 - S_0 \sin\alpha}{(1-\sin\alpha)\tau_y} \qquad \mu = \frac{S_0 - S_1}{(1-\sin\alpha)P_0^{*}(1-\delta)} \tag{4}$$

where α is the angle of the pin with the vertical, S_o is the shear stress between the bottom of the pin and the shoulder with the material, S_1 is the shear stress derived from the pin side and the material, and P_0^{*} is the axial stress result from axial load, as indicates Eq. (5):

$$P_0^{*} = \frac{F_{axial}}{\pi R_{sh}^2} \tag{5}$$

where R_{sh} is the radius of shoulder, and F_{axial} is the maximum axial force during the welding.

Let Ψ be the shear stress ratio obtained by dividing S_o by S_1, this ratio is larger than 1, as the shear stress present between the bottom of the tool and the material is always higher than the one present at its lateral face. Sue et al, also demonstrated that the acceptable range of Ψ should be as Eq. (6) [28].

$$1 < \Psi < \frac{1}{\sin\alpha} \tag{6}$$

Many authors [2, 28] have shown that with decreasing temperature, the yield shear stress at the contact increases. As a result, slip rate reduces so that it would be zero (fully sliding). At this time, according to Eq. (4), Ψ is 1 (the lowest value for Ψ). On the other hand, they approved that by raising temperature, the yield shear stress at the contact decreases. Therefore, slip rate increases so that it would be 1 (fully sticking). That is why Ψ must reach its maximum so that the slip rate gets maximum. Through these explanations, it can be deducted that rising temperature reduces Ψ, decreasing temperature rises Ψ.

The expression of the torque at the shoulder (M_{sh}), pin bottom (M_{bot}) and pin side (M_{ps}) can be written as [2]:

$$M = M_{ps} + M_{bot} + M_{sh} \tag{7}$$

If the corresponding torques are estimated using the equations presented in [2] then Eq. (7) can be reformulated as a linear relation as in Eq. (8):

$$AS_0 + BS_1 = M \tag{8}$$

A and B are two coefficients that reflect the geometrical characteristics of the tool, and can be calculated by Eq. (9):

$$A = \frac{2}{3}\pi\left(R_s^3 - R_1^3 + R_2^3\right) \qquad B = \frac{2}{3}\pi\left(R_2^2 H + 3R_2 H^2 \tan\alpha + H^3 \tan\alpha^3\right) \tag{9}$$

where H is the height of pin, R_1 is the conical pin radius at the shoulder, R_s is the shoulder radius, R_2 is the conical pin radius at the bottom.

According to Eqs. (7) and (9), and the principle that as temperature increases, the ratio of stress Ψ decreases, a descending linear for the ratio of $\frac{S_0}{}$ S_1 was considered. The highest value of Ψ assumed to be nearly $\frac{1}{\sin\alpha}$ ($\Psi_{min} \sim \frac{1}{\sin\alpha}$ at T_{min} =25 °C) and another assumption is that the lowest value of Ψ is closes to 1 ($\Psi_{min} \sim 1$ at T_{max} =500 °C).

By doing so, the maximum and minimum value of Ψ, S_o, and S_1 can be estimated (Fig. 4). It is expected that with increasing temperature (which is associated with decreasing yield stress), regimen sticking/sliding are more likely to occur at the tool/matrix interface [2]. Here the temperature of 500 °C is chosen as the temperature at which the regimen sticking prevail ($\Psi_{min} \sim 1$):

1- Because the value of this temperature is roughly equivalent to 0.9 T_M that is within the predicted range of 0.6 T_M– 0.9 T_M.
2- According to [20] near solidus temperature (502° C) significant softening will occur. It refers to empirical softening regime located 450-500° C.
3- Yielding Stress variations (with high strain rates) are low at temperatures above 450 to 500° C compared to temperatures less than 450 ° C [47].

It is tried to suggest hypothetical distribution of Ψ in a manner that satisfies Eqs. (6–7). Inasmuch yielding shear stress as a function of temperature, changes at 8 levels, the range spanning from S_{1min} to S_{1max} is divided to 8 levels with a constant increment. subsequently S_{0i} and Ψ_i in a manner that satisfies Eqs. (8–9), are calculated at every level. Now eight of Ψ_i s with descending sequence have been introduced as shown in Fig. 4.

If Ψ_i (corresponding temperature is T_i) is the average of the shear stress ratio created by the tool, since the tool/workpiece interface experiences different temperature ranges at any time, average value of δ is $\delta_{ave\ i}$ can be then calculated.

As a result, the friction coefficient $\mu_{avve\ i}$ is determined averagely, according to Eq. (10):

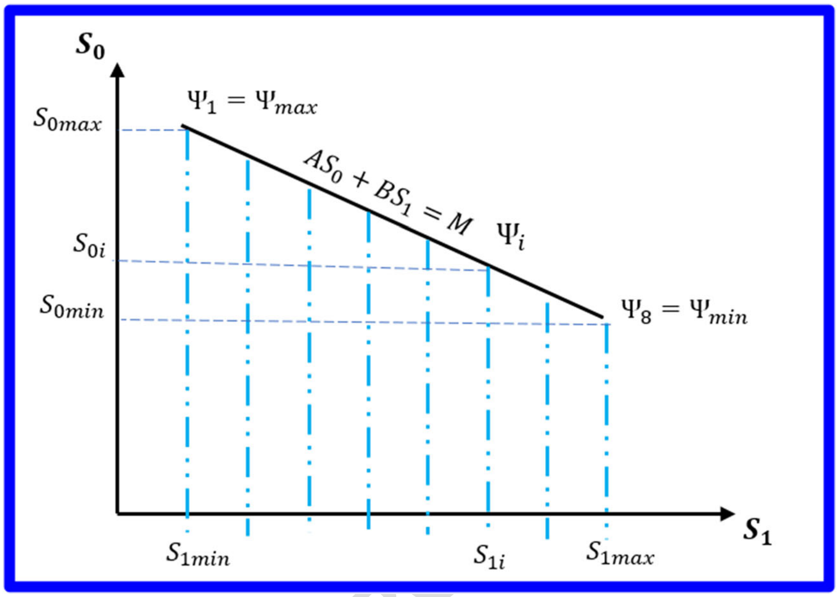

Fig. 4 Estimation of S_{0max}, S_{0min}, S_{1max}, S_{1min}, and Ψ_i s

$$\mu_{ave\ i} = \frac{S_{0i} - S_{1i}}{(1-\sin\alpha) {P_0}^{*}(1-\delta_{ave\ i})} \tag{10}$$

The process above is repeated for all Ψ_i s. For more clarification of friction estimation, the above-mentioned trend has been detailed in a programmable flowchart (Fig. 5). Keep in mind that τ_{yj} (in Fig. 5) is the yield shear stress at the corresponding temperature (strain rare is 10s^{-1}).

2.4 Finite element model description

The heat transfer equation in static Cartesian coordinate system can be written according to Eq. (11):

$$\rho c \frac{\partial T}{\partial t} = \frac{\partial}{\partial x}\left(k_x \frac{\partial T}{\partial x}\right) + \frac{\partial}{\partial y}\left(k_y \frac{\partial T}{\partial y}\right) + \frac{\partial}{\partial z}\left(k_z \frac{\partial T}{\partial z}\right) + \dot{Q}_g \tag{11}$$

where ρ is density, c is specific heat, k is heat conductivity, T is temperature, t is time, x, y, and z are spatial coordinates, and $\dot{Q}_g$ is rate of heat generation.

2.4.1 Heat generation during FSW

Let Q_{tot} be the total heat generated during FSW. It is originated from two sources: frictional heating at the tool/work piece interface (q_f) and plastic energy dissipation due to shearing deformation (q_p).

Heat generated by friction Software ANSYS uses Eq. (12) to calculate local heat generated by friction q_f at the tool/workpiece interfaces [40, 48].

$$q_f = FHTG \times \tau \times \dot{\gamma} \quad , \quad \dot{\gamma} = v_{tool} - v_{matrix} \tag{12}$$

where τ is the equivalent frictional stress, $\dot{\gamma}$ is the slip rate, and *FHTG* is the thermal conversion efficient, that is, the frictional dissipated energy converted into heat and assumed to be 1.

On the other hand, the weight factor for the distribution of heat between contact and target frictional heating energy is considered [40]. Previous works suggested that different fraction of total heat may conduct into the plates during the welding [17, 22]. In the current study, the weight factor is 0.85. Selecting this calibration factor causes the temperature at the contact surface of the pin at the end of the welding process to be equal with the maximum temperature of the plate.

Although some authors [49] claimed that pin and its shape influences material flow, here to prevent mesh distortion and save time solving the problem, the pin tool was not modeled [20]. Instead, its effect was added to the FHTG base value, taking into account that in the literature, it is stated that the ratio of heat generated from the pin (Q_{pin}) to the whole produced heat (Q_{tot}) is between 5% to 20% [15, 16, 50]. In this study, 0.11 is considered, according to Riahi et al. [50].

Heat generated during plastic deformation In a thermoplastic analysis, the stress equation of motion and heat flow conversation equation (first law of thermodynamics) are coupled by the plastic heat density rate $\dot{q}_p$ defined as Eq. (13):

$$\dot{q}_p = \beta \dot{W}_p, \dot{W}_p = \{\sigma\}^T \{\varepsilon_p\} \tag{13}$$

where $\dot{W}_p$ is plastic work rate, $\{\sigma\}$ is stress vector and $\{\varepsilon_p\}$ is plastic strain rate vector and β is fraction of plastic work rate converted to heating. This coefficient is function of strain and

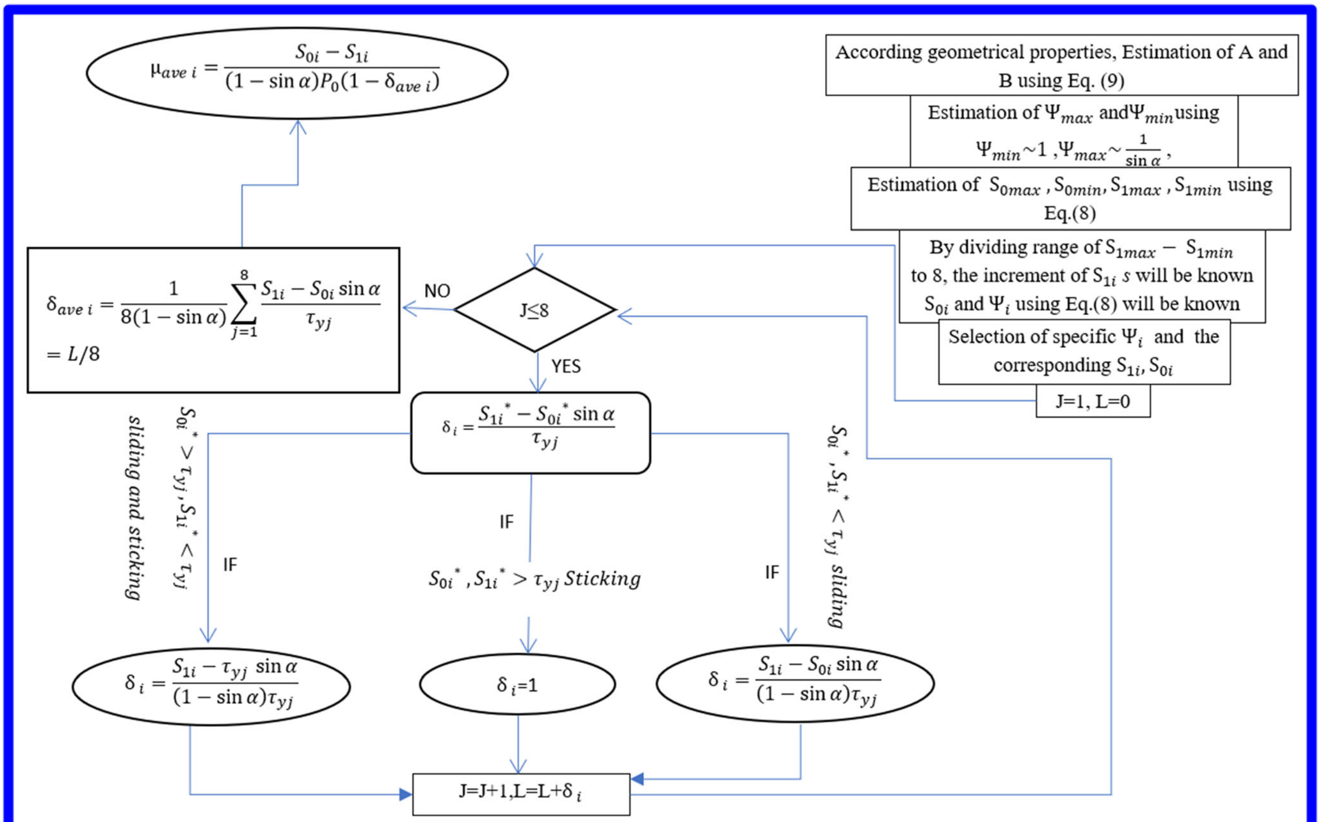

J=	1	2	3	4	5	6	7	8
Temp.	25 °C	100°C	250°C	300°C	350°C	400°C	450°C	500°C
σ_y (MPa)	345	331	296	255	164	124	107	86
τ_{yj} (MPa)	**199.18**	**191.1**	**170.8**	**147.2**	**94.6**	**71.5**	**61.7**	**49.6**

Fig. 5 Programmable flowchart to estimate temperature-dependent friction coefficient

strain rate. Since for the FSW problem high strain and deformation are present and hot deformation microstructures store negligible energy, β was assumed to be 100% or unity [51].

2.4.2 Frictional stress at the contact and modified Coulomb's law

Although the effect of sticking/sliding is taken into account for the estimation of shear stresses S_1, S_0 and subsequently the calculation of friction coefficient, the protocol used by the FEM software to estimate shear stress during sliding condition is:

$$\tau_{con} = \mu\sigma \tag{14}$$

where μ is the friction coefficient (derived Eq. (10)) and σ is the normal stress.

In this study to cover sticking and sliding condition, Coulomb's law will be modified. Since contact shear stress exceeding τ_y is not practicable, the modified Coulomb's law at the contact conditions will be utilized as shown Eq. (15).

$$\tau_{con} = \begin{cases} \mu\sigma & \tau_{max} < \tau_y(T) \\ \tau_y(T) & \tau_{max} \geq \tau_y(T) \end{cases} \tag{15}$$

Eq. (15) as a contact rule is depicted graphically (Fig. 6). As was mentioned above, $\tau_y(T)$ is calculated with Eq. (3). Theses temperature-dependent shear yield stresses are defined at the contact surface and matrix (Table 4).

2.4.3 Thermal boundary condition

The frictional and plastic heat generated during FSW process propagates rapidly into remote region of the plates. On the top and side surfaces of the plates, convection and radiation account for heat loss to the ambient. Conduction losses also occur from the bottom surface of the workpiece to the backing plate [14].

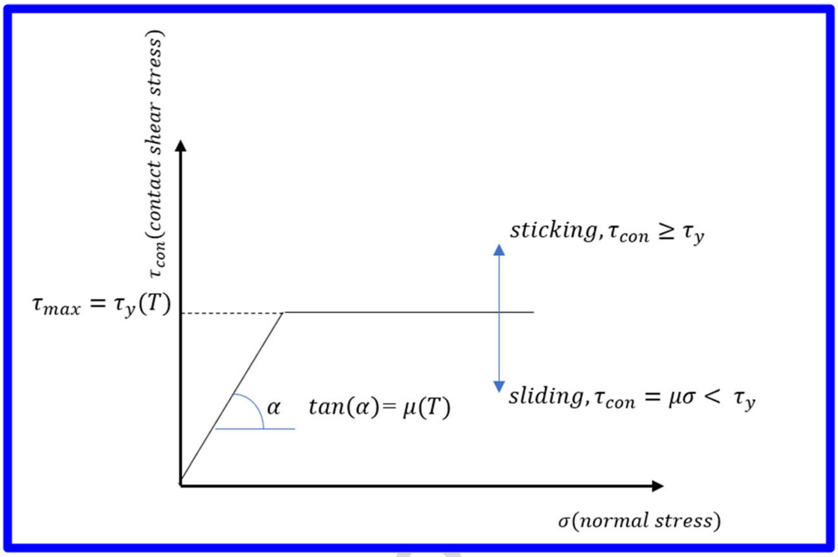

Fig. 6 Modified Coulomb's criterion at the contact surface to represent friction between the FSW tool and the material

A temperature of 25°C is applied on the model as initial condition as Eq. (16)

$$T(x, y, z, t_o) = T_o = 25 \tag{16}$$

where $T(x, y, z, t)$ is the transient temperature field which is function of displacements (x, y, z) and time (t). $T(x, y, z, t)$ is the solution of the governing equation (Eq. (11)).

The boundary condition for heat exchange between the top surface of the workpiece and the surroundings involves the consideration of convective heat transfer (radiation for heat loss was assumed to be negligible) and is given by Eq. (17):

$$-k\frac{\partial T}{\partial z}\Big]_{top} = h_t(T - T_0) \tag{17}$$

In this research, $25\frac{W}{m^2}$ has been used for h_t as heat transfer coefficient. It should be noted that because fixture mechanism used during the process (Fig. 7), provides a slight contact with the top surface of the workpiece (compared to the integrated clamp that constrained about 20 percent of each plate), h_t will be considered as a representative value for the whole top surface. At the side surfaces of the workpiece, the same value of heat transfer was considered. For the heat transfer between the backing plate and bottom of workpiece, the artificial heat transfer coefficient was considered as Eq. (18):

$$-k\frac{\partial T}{\partial z}\Big]_{bottom} = h_b(T - T_0) \tag{18}$$

The desired coefficient h_b is as a function varying with temperature. The conductance coefficient between the backing plate and the workpiece is uncertain, as the large downward pressure below the tool will increase the actual area of contact at the interface and so increase the local rate of heat transfer [52]. In this study, in order to simplify the simulation and calibration of the temperature, the convection between the backing plate and bottom of the workpiece assumed to be constant and is $300\frac{W}{m^2}$

2.4.4 Mechanical boundary condition

During FSW, the top surface of the plates is fixed at four zones. A fixed zone can be represented as a bolt and nut fixed to the clamp. The boundary condition used for the FEM is represented by imposing that the displacement of these nodes is zero. $(U = 0)$ (Fig. 7). On the other hand, the bottom surface of the raw material supported by the backing plate, were assumed to be fixed in the normal direction: $U_z = 0$

2.4.5 FEM simulation

The simulation of FSW has been implemented on a commercially available FEM software ANSYS Mechanical APDL. Based on Lagrangian approach, a 3-D 20-node *SOLID226* element with coupled–field (structural-thermal) capabilities

Table 4 Defining temperature-dependent shear stresses at strain rare of 10s[-1] [30]

Temp.	25 ^{0}C	100°C	250°C	300°C	350°C	400°C	450°C	500°C
σ_y (MPa)	345	331	296	255	164	124	107	86
τ_y (MPa)	199.18	191.1	170.8	147.2	94.6	71.5	61.7	49.6

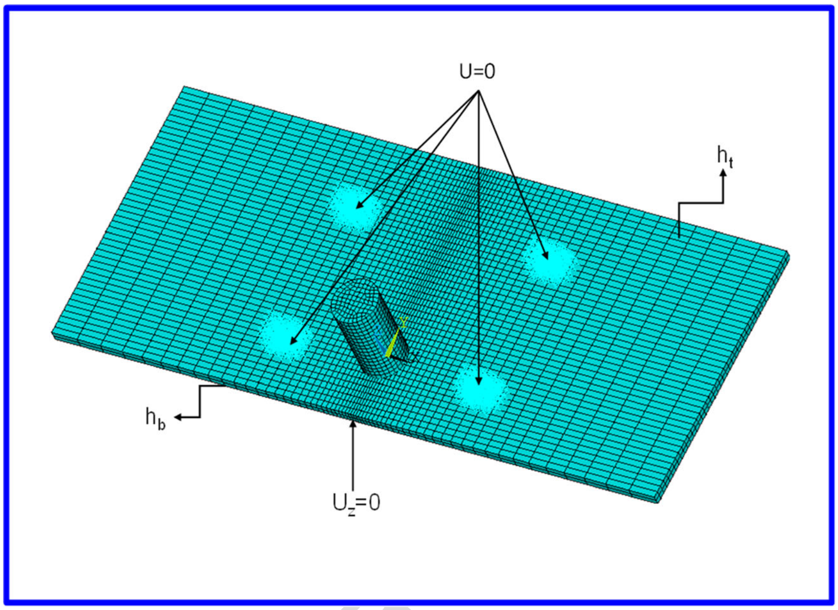

Fig. 7 Display of thermal and mechanical boundary conditions in FEM model

was used. A hexahedral mesh to avoid mesh-orientation dependency with dropped midside nodes was selected, because quadratic shape functions lead to oscillations in thermal solution, leading to nonphysical temperature distribution. To reduce computation time, the regions away from the weld line were modeled with a coarse mesh and a finer mesh has been used in the proximity of the weld line (Fig. 7). For each plate, number of divisions *(NDV)* is 30 with an aspect ratio *(ASR)* of 0.1 along the *X* axis. *NDV* is 44 and *ASR* is 1 along the *Y* axis. Along the thickness (*Z* axis), *NDV* is 3 and *ASR* is 1. The height of the tool is 25 mm and 0.0015 mm has been selected as element size.

Contact element types *CONTA174* and *TARGE170* were used to model the contact between the two plates. To achieve continuous bonding and simulate perfect thermal contact between the plates, a high thermal contact conductance of 2 × $10^6 W/m^2 \circ C$ is determined [40]. Welding occurs after the temperature of the material around the contacting surfaces exceeds the bonding temperature (T_{BN}). At higher temperature than the bonding temperature (approximately 70 % of the workpiece melting point temperature), sticking appears and so contacting surfaces remain joined permanently even after plates get cold. In the current study, according to obtained procedure (like shown in Fig. 5) at the strain rate less than 10 s^{-1}, T_{BN} is assumed to be 350^0C. A standard surface-to-surface contact pair using the same contact element is defined between tool and workpiece. A low thermal contact conductance is specified for this contact pair because most of heat generated transfers to the workpiece. The suggested value is $10 W/m^2$ °C [40].

It should be noted that all required modifications in contact elements have to be done in accordance with Section 2.4.2 and Section 2.3. Accordingly, this simulation includes a subroutine to implement the maximum shear stress at the contact and the friction coefficient as variables with temperature, to meet Coulomb conditions and heat generation distribution. Also, a pilot node is created at the center of the top surface of the tool in order to apply rotation and translation on the tool.

Since the presence of a rigid tool under force axial may causes some difficulties about convergence and illogical response during the simulation, the tool and plates have been considered as deformable parts and the simulation has been done under axial displacement. Therefore, some indentation tests under axial forces of 10 and 13 KN were simulated separately to estimate the maximum displacement of the pilot node. These values (Table 5) were used as input loads during the plunge/dwell stage in each corresponding FSW simulation.

In the current study, according to a Lagrangian model, the whole FSW process has been simulated in three stages (Table 6).

It is worth mentioning that the plunge/dwell stage takes Q4 60 s practically, because rate penetration of 3 mm/min has been considered for all tests due to power limitations of the CNC machine. The full simulation of that stage is time-consuming along with a lack of convergence due to the complexity of heat generation. Therefore, time calibration is the

Table 5 Estimation of maximum displacement pertain to pilot node as plunging load

Force (kN)	Displacement (mm)	Used in tests
10	0.0616	tests (3,4,5)
13	0.0811	tests (1,2)

Table 6 Description of simulation steps during the welding process

Stage number	Stage name	Time step (s)	Loading on pilot node as boundary condition
1	Plunge	1	Axial displacement along Z axis
2	Dwell	4.5	Rotation about Z axis
3	Welding (tests 1, 4)	135	Rotation about Z axis and traversal speed along Y axis
3	Welding (test 3)	90	Rotation about Z axis and traversal speed along Y axis
3	Welding (tests 2, 5)	67.5	Rotation about Z axis and traversal speed along Y axis

process that is necessary to implement when displaying FEM and experimental results. Calibration is performed so that the time reported by the thermocouple for a given point (when the point experiences the maximum temperature) is coincident with the time obtained by the FEM simulation for the same point (when the temperature of that point is the highest).

3 Result and discussion

In order to show the robustness of the model, five weld samples with different welding parameters have been simulated. These procedures are such a way that the effects of rotational and welding speed on the temperature history and heat generation rate have been investigated.

3.1 Axial force and moment within the FSW process

Although in most studies, especially in simulations, the axial force during FSW is assumed to be constant within the process, it actually varies as can be seen in the temporal representations of the axial forces for different tests show in Fig. 8.

At the beginning of the pin penetration into the tool, the temperature is low. More pin penetration requires more axial force because the pin is conical and each moment the projected area in contact is increased until the axial force reaches its maximum value. At this time, due to the heat generated by friction, the yield strength of the material decreases and the material begins to flow beneath the pin and a sudden drop in axial force occurs. As the pin penetrates, the shoulder becomes involved, which increases the projected area in contact in such a way that insufficient heat is provided to flow material, thus increasing the axial force again. After a short time, due to the pin rotation, the temperature rises again and the material resistance decreases and at just this moment, the linear motion of the pin occurs and because here heat generation created while the penetration is constant, the axial force decreases. The maximum value of axial load during welding is considered as the axial force [28].

An average value of the torque during the welding (not Plunge and Dwell) obtained from Eq. 1 was used. For each tested condition, 4 replications were conducted for the sake of repeatability. These results have been detailed in Table 7. It shows that the higher tool traverse speed, the more torque needed. Meanwhile increasing rotational speed result in reduction in torque and maximum axial force.

3.2 Temperature-dependent friction coefficient

If the temperature-dependent friction coefficient estimation protocol is implemented for all tests, the friction coefficient can be plotted in terms of the shear stress ratio (Fig. 9-a). It is in harmony with results presented by [28]. If the temperature corresponding to the shear stress ratio is used in this figure, Fig. 9-b will be obtained. These figures state that with increasing temperature in a constant Ψ, δ raises. In a constant temperature, reduction in Ψ leads to increase in δ as well. The faster the tool rotates, the lower friction coefficient. While with increasing welding speed, the friction coefficient raises. Figure 9-b shows that the rotational speed compared to the welding speed has a predominant effect on the coefficient of friction. For this reason, a mean diagram of the temperature-dependent friction distribution can be considered for simplicity in tests with the same rotational speed and different welding speed.

3.3 Temperature measuring

3.3.1 General overview

In order to show the temperature field graphically, one of the welding simulations performed with welding speed of 40 mm/min and rotational speed of 1100 min^{-1} when the tool located in the middle of the welding path is shown in Fig. 10. To show the maximum temperature of the workpiece, the tool is deliberately not displayed. The temperature contour lines are close to circular as the welding speed as slow as 20 mm/min to 40 mm/min, for all tests [53]. Because in the TMAZ, the heat produced by plastic deformation was diminished (due to the omission of the pin in the simulation). In the magnified section A-A, the distribution of the temperature field is almost asymmetric (this is clearer in Fig. 12), and it depicts the temperature difference between the advancing and retarding sides (about

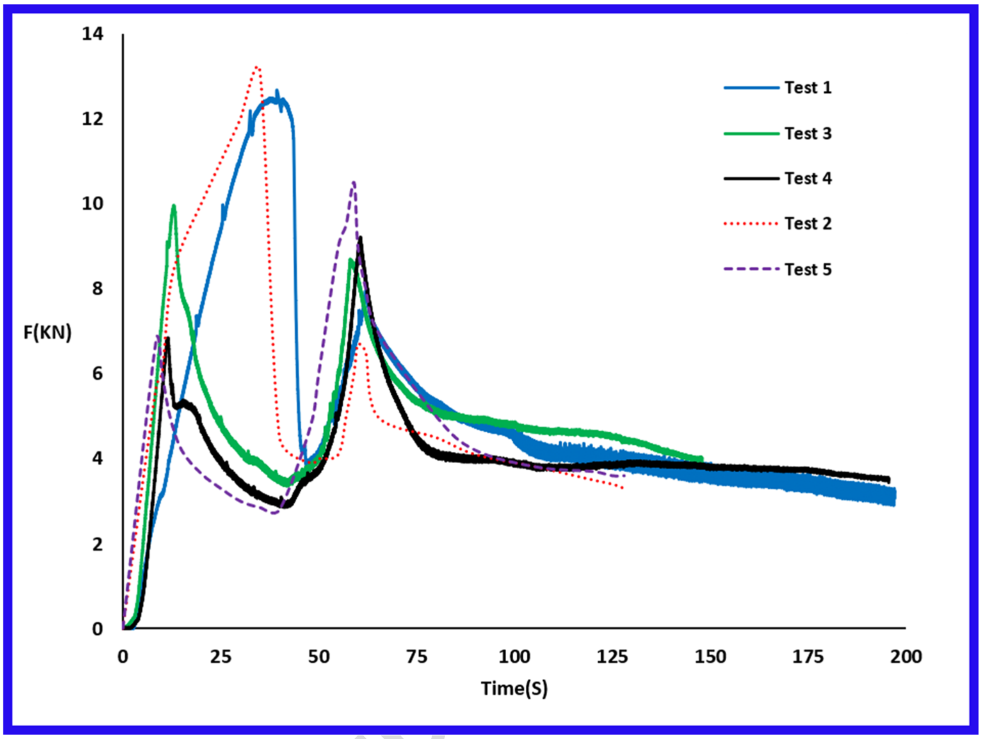

Fig. 8 Measured axial forces during the FSW process

4-6^{0}C). Although this value reaches 13 to 15°C experimentally.

3.3.2 Time-dependent temperature evolution

Temperature histories recorded by thermocouples and FEM results are shown in Fig. 11. According to Fig. 2-b, the thermocouple was located in the middle of the weld line during the experimental phase and 16.2mm far from the centerline, recording the temperature at the advancing of the plates. It is worth mentioning that in Fig. 11, time is calibrated. Figure 11 reflects the effect of the rotational and welding speed on the temperature histories experimentally, compared to the FEM results.

It can also be seen that the higher the rotational speed, the higher the maximum temperature. In most cases, the maximum deviation between the experimental data and FEM results appears in the time interval 5 to 18 s (in most cases). This is because plunge/dwell takes 60 s experimentally, while this time is 5.5 s for FEM simulation. Accordingly, the amount of heat generation due to the experimental test at the end of the dwell stage is more than the corresponding simulation, due to the fact that the experiment takes almost tenfold compared to the simulation. Consequently, further increase in temperature occurs in the experiment during fifth to eighteenth seconds.

Table 7 Experimental force and moment during FSW

Test	Maximum force (KN)	Average torque (N-m)
1	13	21.3
2	13	22
3	10	16.1
4	10	12.7
5	10	13.54

Of course, this deviation in simulation during plunge/dwell can be reduced by increasing the dwell duration in modeling. Here, the dwell duration is restricted to the time in which the maximum temperature has not changed. As shown in Fig. 11, test 2, test 1, test 3, test 5, and test 4 will reach the temperature equilibrium with the environment, respectively.

Maximum temperatures recorded by thermocouples from FEM simulations slightly deviate in all tests. These results have been detailed in Table 8.

By comparing test 1 to test 2 and test 4 to test 5 in Table 8, it can also be observed that as the welding speed decreases, the maximum temperature rises for each point, which is in harmony with previous articles [9]. For instance, when decreased from 40 to 20 mm/min, regardless of the rotational, temperature rises at the modeling nodes 4-5 °C (test 1 and 2) and 6–8 °C (test 4 and 5) respectively. The displayed temperature histories for all tests also show that as the tool approaches the traverse line, the temperature increases and when the tool reaches the traverse line and passes through it the temperature starts to decrease.

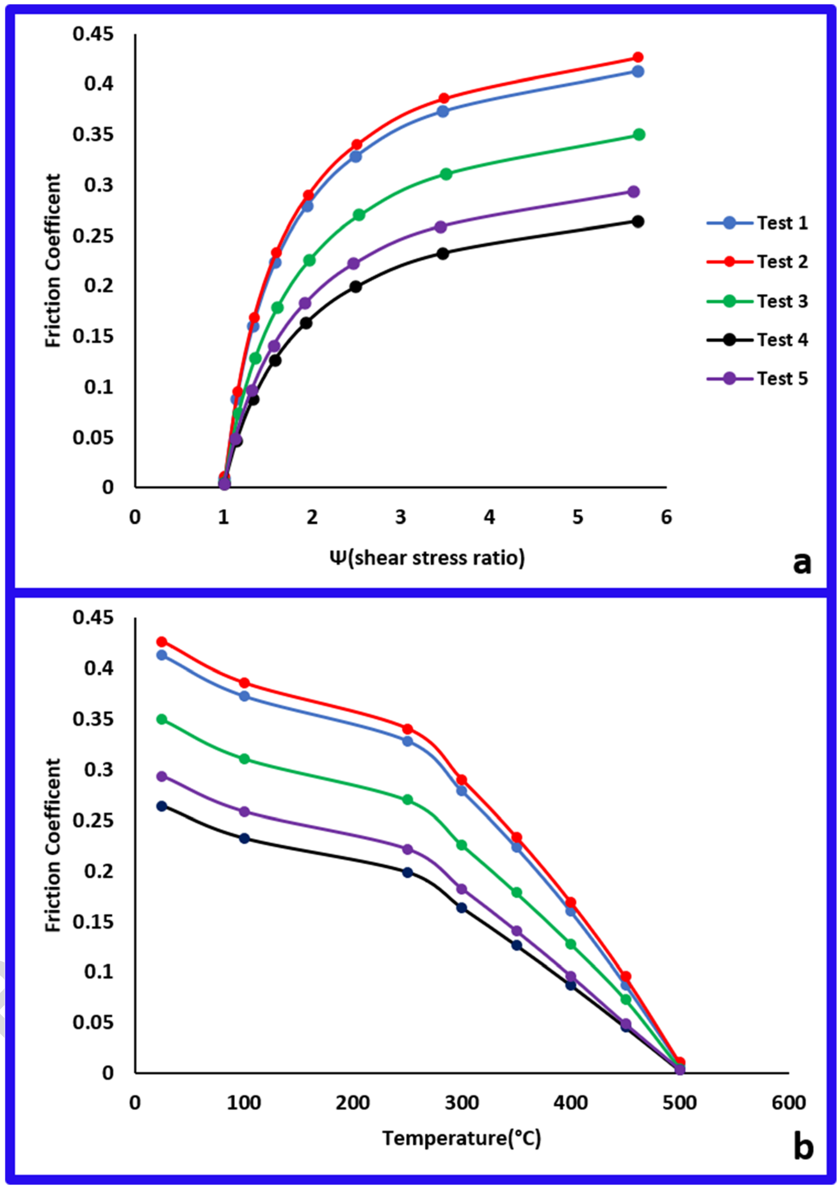

Fig. 9 (**a**) Variation of friction coefficient versus shear stress ratio (**b**) Temperature-dependent friction coefficients

3.3.3 Spatial temperature distribution

Figure 12 represents the temperature distribution derived from the different simulations, compared to the experimental measurements. Experimental tests in this study have shown that the temperature gradient difference among the tests is more noticeable up to a distance of 30 mm from the center. For this reason, the range of distance covered by the experimental measurements is from X=−30 to X=30 [54]. The average temperature of the tool at the point of contact with a point along the path in the trailing edge (close to the tool edge) is considered as the temperature of the welding center. the values obtained are consistent with [55]. These graphs show that as approaching the centerline along the traverse direction, temperature raises. The highest values along those paths are located in the advancing side at the periphery of shoulder, approximately 5–6 mm from the tool center. This location is more than pin radius and less than shoulder radius as observed in other works [50, 56]. after the plunge/dwell stage, the maximum temperatures observed for tests 1 to 5 changes up to 30 °C during the welding. However, these numbers are slightly less than the maximum values created by the tool in simulation, because the highest values of temperature located on the quarter of the shoulder between the trailing edge and advancing side which are not laid in the traverse path through the middle of the workpiece and tool which is in conformity with the work carried out by H. Su et al. [28].

Error analysis between experimental and FEA results is listed in Table 8. As can be seen from the Table 8, the FEA results are more consistent with experiments in advancing side and the error amount is lower. As the distance from the welding line increases, the temperature

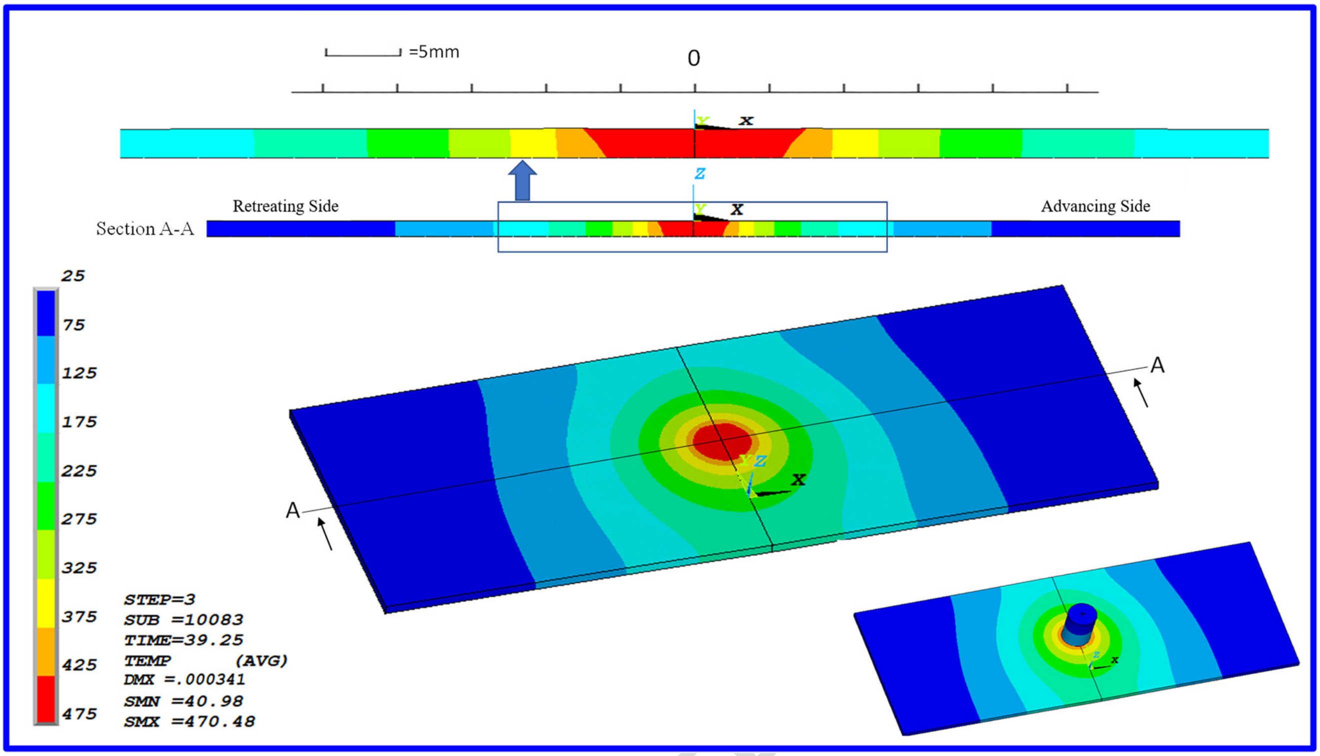

Fig. 10 Obtained temperature field in the test 5 (ω = 1100 min^{-1}, V = 40 mm/min) from FEM model

difference between the advancing and retarding side decreases. Figure 12-a also shows simulated temperature profiles at three different layers (along the thickness) for test 2 and test 5. From the top layer (z=0) to the bottom layer (z=-3mm), the maximum temperature drops by about 21 °C. The greatest reduction in temperature occurs from the top layer to the middle layer. The temperature difference between the advancing side and retarding side decreases through the thickness so that the temperature profile on the bottom layer is symmetric.

Table 8 also shows that peak temperature among all tests appears in test 4 (with the highest rotational speed and the lowest welding speed, axial force and torque). It is in good agreement with [57].

3.3.4 Maximum temperature at the tool-material interface

The issue of predicting the highest temperature created by the tool at a certain time was tackled, by incorporating a special subroutine to identify the elements in contact

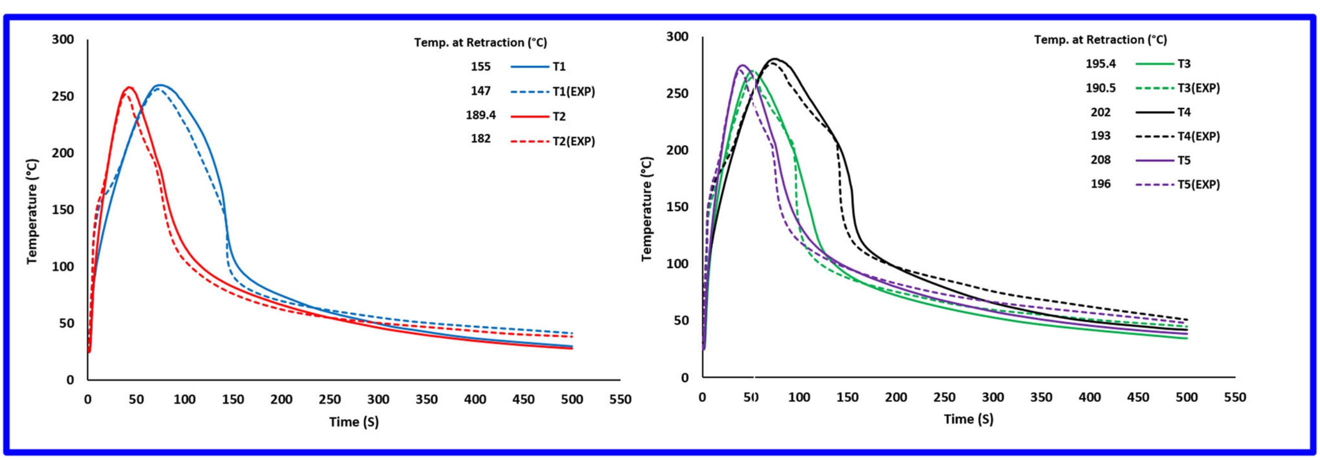

Fig. 11 Comparison of temperature histories obtained from thermocouples and simulations. Recorded temperature up to 500 s in advancing side at y= 22.5 mm, x= 16.2 mm

Table 8 Error analysis (FEM results and Experiments) along the traverse path (y=22.5mm)

Test	AS (7.5,16.2,20,29)mm EXP	Error(%)	RS(7.5,16.2,20,29)mm EXP	Error(%)	X=0 EXP	Error(%)	Max. Temp
1	399,259.3,225.3,165.4	0.5,1.2,2.9, 4.4	393.5,254.8,221.3,163.7	1.9,3.07,3.4,5.1	437.5	0.3	446
	397,256.2,218.9,158.3		384,247.2,214,155.7		436		
2	394,256.1,221.2,161.3	0.2,1.6,2.1,4	388.7,252.1,217.2,159.6	2.1,3.7,3.1,5.6	433.4	0.5	441
	393,252,216.6,155		380.5,243,210.5,151		431		
3	411.5,269.4,235.3,174	2.1,2.3,2.1, 1.5	406.5,265.2,231.8,172.5	4,5.1,4,3.1	450.4	0.6	461
	403,263.2,230.4,171.3		390.7,252,222.7,167.3		453.3		
4	425.3,280.2,242,178.54	1.2,1.8,1.2, 2.4	420,275.1,238.5,177.1	2.9,4.6,2.9,3.3	465.4	1.1	477
	420,275.2,239.1,174.3		408,263,231.6,171.3		470.7		
5	419,274,236,172.5	1.1,1.4,1.2, 2.6	415,269,232.5,171.1	3.2,4.6,2.9,3.6	459.4	1.4	471
	414.3,270,233.7,168		402.7,257.6,225.9,165		466		

between two solids (tool and workpiece). This subroutine computes at a certain time step all contact elements and restores those elements whose reaction forces are not zero. Figure 13-a shows the temperature field of the elements in contact with the tool for test 2 (ω = 550 min^{-1}, V = 40 mm/min). The maximum and minimum temperatures are specified. As seen in Fig. 13-a, the temperature profile is skewed toward the advancing side, confirming the observation made above about the asymmetry of the distribution. The highest temperature appeared at the distance of 4.72 mm from the tool center and located in the fourth quarter between the trailing edge and the advancing side.

The lowest temperature appeared in the second quarter between the leading edge and the retarding side. The maximum temperatures occurred for all tests (1 to 5) in modeling when the tool reached to the middle of welding length are listed in Table 8 (last column of the Table 8). All these values are lower than the solidus temperature of 2024 aluminum alloy which are about 80 to 90% of melting point and consistent with empirical values [27, 45].

In addition to the axial forces, experimental lateral and longitudinal forces are estimated in this study. Figure 13-b shows for test 4 that these forces remain almost constant during linear the welding. The forces are expressed in the coordinate system attached to the Kistler kit shown in Fig. 2-b. They could be expressed in the coordinate system of FEM simulation (force map of the tool in Fig. 13-b). For all tests, this data summarized in Table 9. Tangential force (R_t) due to forces (acting on the contact plane) is shown in Fig. 13-b. Since R_t is proportional to the amount of friction coefficient [31], it could be realized that the highest frictional stress occurs at the quarter of the shoulder between the trailing edge and advancing side. That is why the maximum temperature at the interface shoulder/workpiece at the mentioned quarter of the tool is expected to appear which is in conformity with the simulated temperature map in Fig. 13-a for test 1 to 5.

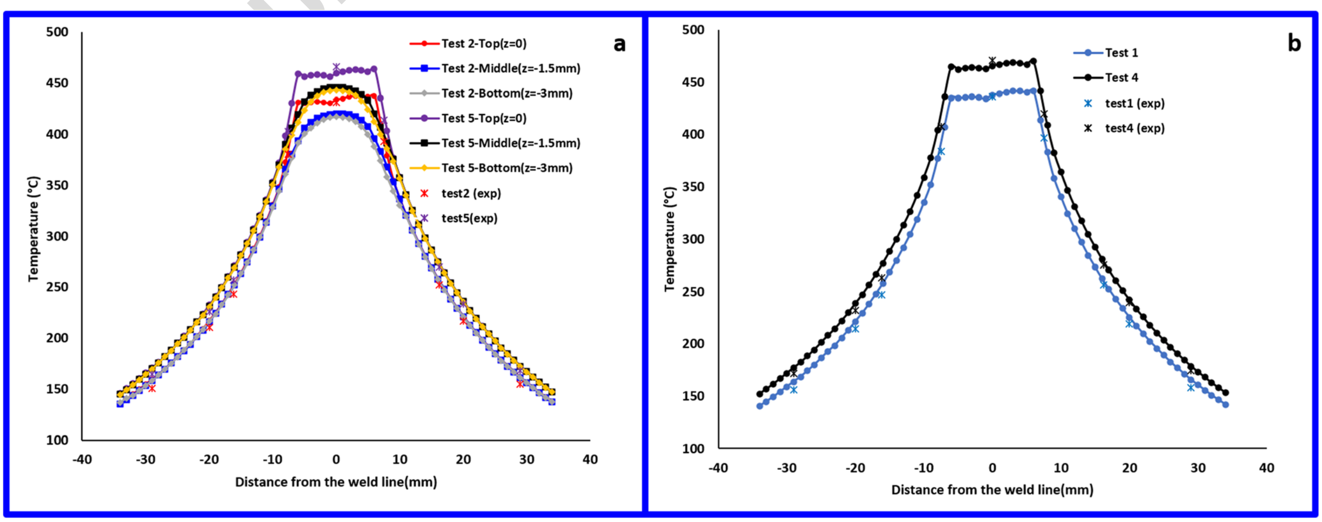

Fig. 12 Comparison of temperature changes obtained from thermocouples and thermometer and simulations along traverse path (when the pin reached to the middle of the weld line y=22.5mm, x,z=0). (a). test 2 and test 5 (b). test 1 and test 4

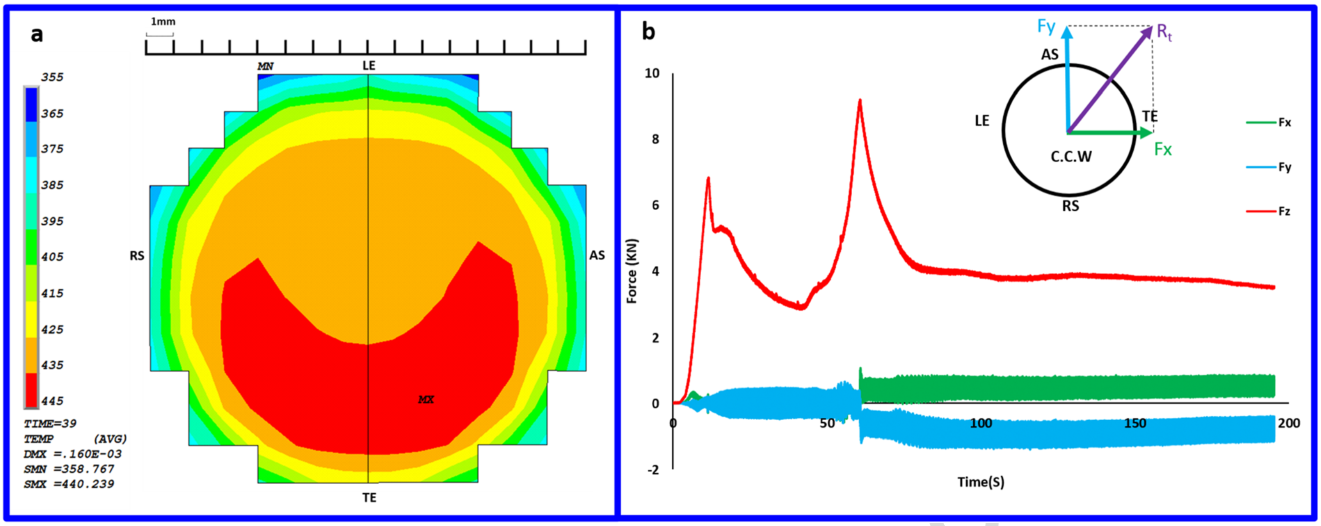

Fig. 13 (**a**) Simulated temperature map of tool / workpiece interface for test 2. (**b**) Output of axial and lateral forces for test 4 (expressed in coordinate-system attached to Kistler)

3.4 Frictional heat dissipation

It was mentioned earlier, since the Lagrangian approach applied for the simulations, modeling of the pin causes high distortion and divergence problem. So, it was neglected in the simulation and to take account for the effect of the pin in heat generated by the shoulder, obtained ratio based on Ref [50] is used to multiply heat generated by the shoulder. By doing so, deformation plastic is limited to the interface between tool/workpiece at the top rather than whole nugget zone. Therefore, heat generated by the deformation plastic has been underestimated

Although some researchers reported that plastic deformation accounts for up to 4.4% of the total heat dissipation [58], the current model shows that it is not higher than 0.4%. For this reason, the main source of heat generation considered in the model is frictional heat.

At this point, by applying a subroutine the rate of heat generated on the workpiece (q_c) is estimated. q_c is the fraction of frictional heat generated (q_f) obtained by multiplying FWGT by q_f . During the early welding stage (plunge / dwell), heat generated is not balanced with the dissipated heat, the balance is established later during the welding process [59]. In Fig. 14-a, frictional heat generation rate for all tests is shown. At the beginning of the plunge/dwell phase, heat generated by friction is dominant. As the tool rotates, the temperature increases and the material at the contact surface become softer and then at certain temperature (T_f) the sticking condition appears. It is here that a sharp drop in frictional heat generated occurs. Particularly, the higher the rotational speed, the sharper the drop (Fig. 14-a). Simulations show that the higher the rotational speed, the faster the sticking conditions occur and this certain temperature is higher.

As can be seen, the maximum heat dissipation rate occurs during the plunge/dwell stage. The result data in Table 10 show that by increasing the rotational speed from 550 min^{-1} to 825 min^{-1} and then up to 1100 min^{-1}, the frictional heat dissipation rate at the plunge stage is raised 41% and 21% respectively. Since during the linear welding, an estimated mean value for the whole process is equal to the average of data from 5.5 to 20 s, a stabilized value as frictional heat generation rate was considered. By increasing rotational speed according to the schedule, the frictional heat dissipation rate during linear welding increased 25% and 10.5%, respectively. These results are in harmony with obtained data for frictional heat generation by Su et al [28]. Table 10 also shows that the higher rotational speed, the more frictional heat generation. It could be realized that the more welding speed, the higher frictional heat generation rate which is in conformity with the result reported by Chao et al [16]. It is related to the fact that the higher the welding speed, the high-temperature zone under sticking decreases (compared to the lower welding speed case) and subsequently friction coefficient increases. It could be noticed that the higher the welding

Table 9 Experimental lateral forces during the welding

Test	Fx (mean) (N)	Fy (mean) (N)
1	1215	-680
2	1262	-710
3	1175	-598.4
4	1037	-517
5	1110	-567

 JrnlID 170_ArtID 7184_Proof# 1 - 09/05/2021

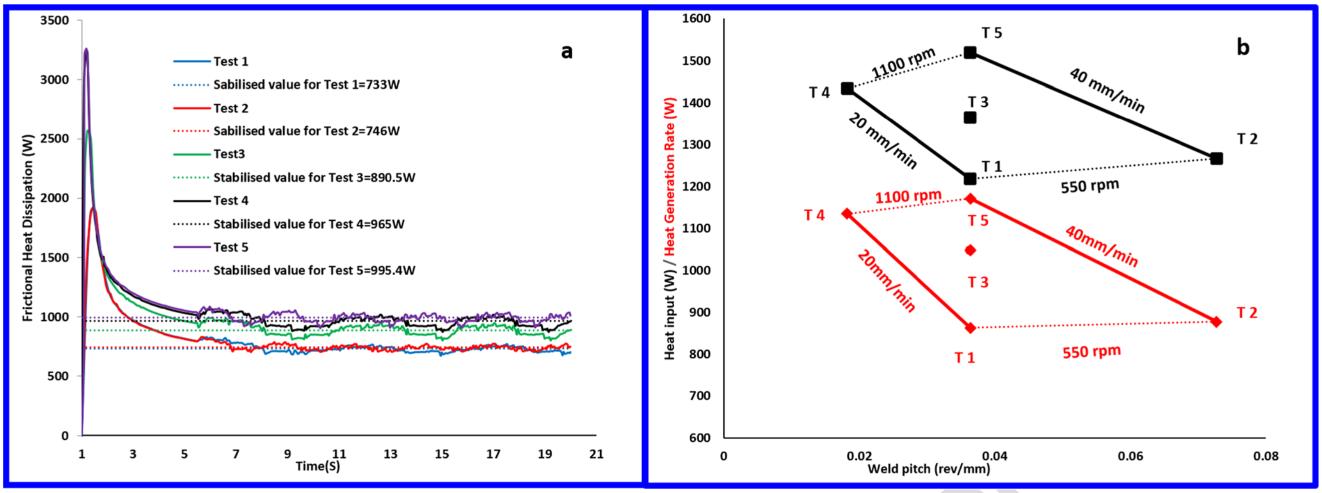

Fig. 14 Variation and comparison of (a) frictional heat dissipation rate in the workpiece and (b) heat input and total heat generation rate during the welding

speed, the more torque required for the FSW process (Table 7) and then more friction according to Fig. 9-b. When welding speed is raised from 20 to 40 mm/min Frictional heat generation rate increased about 1.7% and 3% for the rotational speed of 550 min^{-1} and 1100 min^{-1}, respectively.

Figure 14-b confirms that the rotational speed is the dominant factor to increase the heat input and frictional heat generated. It is in agreement with [60]. At the same weld pitch, with increasing rotational speed (free of welding speed), the heat input and heat generation increase. These values also raise as the both rotational and welding speed are increased. In both graphs (shown in Fig. 14-b) maximum and minimum values are for test 5 (with the highest rotational and welding speed) and test 1(with the lowest values of speed), respectively. these findings are in harmony with [52].

If f is fraction of total heat generated to heat input (power input), Table 10 shows that f decreases as the welding speed raises and f increases as the rotational speed is higher. By assuming that the hot deformation energy store is negligible (β=1) we conclude that at a common f (for example f=0.8) for all tests, the required heat due to deformation plastic (q_p) decreases as the rotational speed increases. Meanwhile, q_p raises as the welding speed is higher.

Table 10 Estimation of frictional heat generated and heat input for welding schedules

Test	Heat input(W)	q_c (W)	q_f (W)	f	q_p (W): f=0.8
1	1217.5	733	862.3	0.7	111.6
2	1266.4	746	877.6	0.69	135.5
3	1364.3	890	1047	0.76	44.4
4	1433.4	964	1134.1	0.79	12.6
5	1519.7	995	1170.5	0.77	45.2

4 Conclusions

The work presented in this study encompasses a range of empirical tests, theoretical relationships, and FEM simulations to investigate the effects of two parameters on friction stir welding, namely the welding speed and rotational speed. At the same time, this research introduces an improved method for estimating the temperature-dependent friction coefficient that plays a significant role in heat generation. The finite element model introduced in this paper has proven to deliver successful results about the FSW process of AA2024-T3 aluminum plates. The conclusions in this work can be summarized as follows:

1. This study introduces temperature-dependent multilinear isotropic hardening as a plasticity model. The robust model that is able to use experimental data. Consistency of simulation results with experiments shows that the compressive stress-strain data at a strain rate of $10s^{-1}$ can deliver a good approximation of strain rate-dependent plastic behavior in the aluminum alloy FSW process.
2. Given that the variable torque is assumed to be a constant mean throughout the process, the stress ratio of S_0 to S_1 decreases linearly with increasing temperature.
3. In the beginning of the process when the temperature is low, the difference in friction coefficients at different rotational speed is noticeable. As the temperature raises (300<T<350°C) the sticking will be dominant in contact. The difference between the friction coefficients decreases as the temperature raises. In other words, the coefficient friction at the high temperatures is almost the same at different rotational speeds.
4. Simulations show that the maximum temperature is located in the fourth quarter between the trailing edge and the advancing side. Experimental estimation of tangential

force direction (that is proportional to the friction force) approves that the friction force in this area is maximum then the maximum temperature is expected to appear in this zone (Fig .13-b). In these tests, created lateral forces are greater than the longitudinal forces and are approximately twice that.

5. With increasing the rotational speed, the torque required to perform the FSW process successfully is reduced, the heat generation and heat input rises. On the other hand, increasing the welding speed causes an increase in the required torque, the higher production of heat and heat input. Of these two parameters, the rotational speed is the dominant parameter in effect.

Author contribution Conceptualization, S.H., M.Z., J.A.T.-R., and R.J.-M.; Methodology, R.J., M.Z., C.A. and J.A.T-R; Software, S.H. and C.A.; Validation, C.A., J.A.T.-R., and R.J.-M.; Formal Analysis, C.A., J.A.T.-R., and R.J.-M.; Investigation, R.J.-M., J.A.T.-R., and C.A.; Resources, J.A.T.-R., and R.J.-M.; Data Curation, S.H., M.Z., and C.A.; Writing-Original Draft Preparation, C.A.; Writing-Review & Editing, J.A.T.-R., and R.J.-M.; Visualization, C.A., S.H., and M.Z.; Supervision, S.H., M.Z., J.A.T.-R., and R.J.-M.; Project Administration, J.A.T.-R., Funding Acquisition, J.A.T.-R., R.J.-M.

Funding Financial support for this study was provided by the Iran Ministry of Science Research and Technology, which is greatly appreciated.

Data availability The raw/processed data required to reproduce these findings cannot be shared at this time as the data also forms part of an ongoing study.

Declarations

Ethics approval This manuscript has not be submitted to another journal for simultaneous consideration. The submitted work is original and not have been published elsewhere in any form or language (partially or in full).

Conflict of interest The authors declare no competing interests.

References

1. Threadgill PL, Leonard AJ, Shercliff HR, Withers PJ (2009) Friction stir welding of aluminium alloys. International. Materials Reviews 54(2):49–93. https://doi.org/10.1179/174328009X411136
2. Schmidt H, Hattel J, Wert J (2003) An analytical model for the heat generation in friction stir welding. Model Simul Mater Sci Eng 12(1):143. https://doi.org/10.1088/0965-0393/12/1/013
3. Nandan R, DebRoy T, Bhadeshia HK (2008) Recent advances in friction-stir welding–process, weldment structure and properties. Prog Mater Sci 53(6):980–1023. https://doi.org/10.1016/j.pmatsci.2008.05.001
4. Lambiase F, Grossi V, Paoletti A (2019) Advanced mechanical characterization of friction stir welds made on polycarbonate. Int J Adv Manuf Technol 104(5):2089–2102. https://doi.org/10.1007/s00170-019-04006-4
5. Huang Y, Meng X, Xie Y, Wan L, Lv Z, Cao J, Feng J (2018) Friction stir welding/processing of polymers and polymer matrix composites. Compos A: Appl Sci Manuf 105:235–257. https://doi.org/10.1016/j.compositesa.2017.12.005
6. Vakili-Tahami F, Adibeig MR, Hassanifard S (2019) Optimizing creep lifetime of friction stir welded PMMA pipes subjected to combined loadings using rheological model. Polym Test 79:106049. https://doi.org/10.1016/j.polymertesting.2019.106049
7. Adibeig MR, Hassanifard S, Vakili-Tahami F, Hattel JH (2018) Experimental investigation of tensile strength of friction stir welded butt joints on PMMA. Materials Today Communications 17:238–245. https://doi.org/10.1016/j.mtcomm.2018.09.009
8. Eslami S, Miranda JF, Mourão L, Tavares PJ, Moreira PMGP (2018) Polyethylene friction stir welding parameter optimization and temperature characterization. Int J Adv Manuf Technol 99(1):127–136. https://doi.org/10.1007/s00170-018-2504-x
9. Rahmi M, Abbasi M (2017) Friction stir vibration welding process: modified version of friction stir welding process. Int J Adv Manuf Technol 90(1-4):141–151. https://doi.org/10.1007/s00170-016-9383-9
10. Abbasi M, Givi M, Ramazani A (2019) Friction stir vibration processing: a new method to improve the microstructure and mechanical properties of Al5052/SiC surface nanocomposite layer. Int J Adv Manuf Technol 100(5-8):1463–1473. https://doi.org/10.1007/s00170-018-2783-2
11. Zhu Z, Wang M, Zhang H, Zhang X, Yu T, Wu Z (2017) A finite element model to simulate defect formation during friction stir welding. Metals 7(7):256. https://doi.org/10.3390/met7070256
12. Soundararajan V, Zekovic S, Kovacevic R (2005) Thermo-mechanical model with adaptive boundary conditions for friction stir welding of Al 6061. Int J Mach Tools Manuf 45(14):1577–1587. https://doi.org/10.1016/j.ijmachtools.2005.02.008
13. Song M, Kovacevic R (2003) Thermal modeling of friction stir welding in a moving coordinate system and its validation. Int J Mach Tools Manuf 43(6):605–615. https://doi.org/10.1016/S0890-6955(03)00022-1
14. Zhu XK, & Chao YJ (2004) Numerical simulation of transient temperature and residual stresses in friction stir welding of 304L stainless steel. J Mater Process Technol 46(2): 263-272.10.1016/j.jmatprotec.2003.10.025
15. Schmidt HB, Hattel JH (2008) Thermal modelling of friction stir welding. Scr Mater 58(5):332–337. https://doi.org/10.1016/j.scriptamat.2007.10.008
16. Chao YJ, Qi X, Tang W (2003) Heat transfer in friction stir welding—experimental and numerical studies. J Manuf Sci Eng 125(1):138–145. https://doi.org/10.1115/1.1537741
17. Chen CM, Kovacevic R (2003) Finite element modeling of friction stir welding—thermal and thermomechanical analysis. Int J Mach Tools Manuf 43(13):1319–1326. https://doi.org/10.1016/S0890-6955(03)00158-5
18. Hamilton C, Sommers A, Dymek S (2009) A thermal model of friction stir welding applied to Sc-modified Al–Zn–Mg–Cu alloy extrusions. Int J Mach Tools Manuf 49(3-4):230–238. https://doi.org/10.1016/j.ijmachtools.2008.11.004
19. Khandkar MZH, Khan JA, Reynolds AP (2003) Prediction of temperature distribution and thermal history during friction stir welding: input torque-based model. Sci Technol Weld Join 8(3):165–174. https://doi.org/10.1179/136217103225010943
20. Colegrove PA, Shercliff HR, Zettler R (2007) Model for predicting heat generation and temperature in friction stir welding from the material properties. Sci Technol Weld Join 12(4):284–297. https://doi.org/10.1179/174329307X197539
21. Colegrove PA, Shercliff HR (2006) CFD modelling of friction stir welding of thick plate 7449 aluminium alloy. Sci Technol Weld Join 11(4):429–441. https://doi.org/10.1179/174329306X107700

22. Ulysse P (2002) Three-dimensional modeling of the friction stir-welding process. Int J Mach Tools Manuf 42(14):1549–1557. https://doi.org/10.1016/S0890-6955(02)00114-1
23. Heurtier P, Jones M, Desrayaud C, Driver JH, Montheillet F, Allehaux D (2006) Mechanical and thermal modelling of friction stir welding. J Mater Process Technol 171(3):348–357. https://doi.org/10.1016/j.jmatprotec.2005.07.014
24. De Saracibar CA, Chiumenti M, Cervera M, Dialami N, Seret A (2014) Computational modeling and sub-grid scale stabilization of incompressibility and convection in the numerical simulation of friction stir welding processes. Archives of Computational Methods in Engineering 21(1):3–37. https://doi.org/10.1007/s11831-014-9094-z
25. Bussetta P, Dialami N, Chiumenti M, Agelet de Saracibar C, Cervera M, Ponthot JP (2015) 3D numerical models of FSW processes with non-cylindrical pin. Advances in Materials and Processing Technologies 1(3-4):275–287. https://doi.org/10.1080/2374068X.2015.1121035
26. Meyghani B, Awang MB, Emamian S, Akinlabi ET (2018) A comparison between temperature dependent and constant young's modulus values in investigating the effect of the process parameters on thermal behaviour during friction stir welding. Mater Werkst 49(4):427–434. https://doi.org/10.1002/mawe.201700255
27. Song P, Li W, Wang X, Xu W (2019) Study on mechanical properties and constitutive model of 5052 aluminium alloy. Mater Sci Technol 35(8):916–924. https://doi.org/10.1080/02670836.2019.1596611
28. Su H, Wu CS, Pittner A, Rethmeier M (2014) Thermal energy generation and distribution in friction stir welding of aluminum alloys. Energy 77:720–731. https://doi.org/10.1016/j.energy.2014.09.045
29. Rasaee S, Mirzaei AH (2019) Constitutive Modeling of 2024 Aluminum Alloy Based on the Johnson–Cook Model. Trans Indian Inst Metals 72(4):1023–1030. https://doi.org/10.1007/s12666-019-01576-5
30. Trimble D, O'DONNELL GE (2016) Flow stress prediction for hot deformation processing of 2024Al-T3 alloy. Trans Nonferrous Metals Soc China 26(5):1232–1250. https://doi.org/10.1016/S1003-6326(16)64194-8
31. Mijajlović MM, Pavlović NT, Jovanović SV, Jovanović DS, Milčić MD (2012) Experimental studies of parameters affecting the heat generation in friction stir welding process. Therm Sci 16(2):351–362. https://doi.org/10.2298/TSCI120430174M
32. Meyghani B, Awang M, Emamian S, Khalid NM (2017) Developing a finite element model for thermal analysis of friction stir welding by calculating temperature dependent friction coefficient. In 2nd international conference on mechanical, manufacturing and process plant engineering, Singapore 107-126. https://doi.org/10.1007/978-981-10-4232-4_9
33. Mishra RS, Ma ZY (2005) Friction stir welding and processing Materials science and engineering: R: reports 50(1-2):1-7810.1016/j.mser.2005.07.001
34. Chang CI, Lee CJ, Huang JC (2004) Relationship between grain size and Zener–Holloman parameter during friction stir processing in AZ31 Mg alloys. Scr Mater 51(6):509–514. https://doi.org/10.1016/j.scriptamat.2004.05.043
35. Chen ZW, Cui S (2009) Strain and strain rate during friction stir welding/processing of Al-7Si-0.3 Mg alloy. In IOP Conference Series: Materials Science and Engineering 4(1):012026. https://doi.org/10.1088/1757-899X/4/1/012026
36. Masaki K, Sato YS, Maeda M, Kokawa H (2008) Experimental simulation of recrystallized microstructure in friction stir welded Al alloy using a plane-strain compression test. Scr Mater 58(5):355–360. https://doi.org/10.1016/j.scriptamat.2007.09.056
37. Arora A, Zhang Z, De A, DebRoy T (2009) Strains and strain rates during friction stir welding. Scr Mater 61(9):863–866. https://doi.org/10.1016/j.scriptamat.2009.07.015
38. Khan NZ, Bajaj D, Siddiquee AN, Khan ZA, Abidi MH, Umer U, Alkhalefah H (2019) Investigation on Effect of Strain Rate and Heat Generation on Traverse Force in FSW of Dissimilar Aerospace Grade Aluminium Alloys. Materials 12(10):1641. https://doi.org/10.3390/ma12101641
39. Zhang P, Guo N, Chen G, Meng Q, Dong C, Zhou L, Feng J (2014) Plastic deformation behavior of the friction stir welded AA2024 aluminum alloy. Int J Adv Manuf Technol 74(5-8):673–679. https://doi.org/10.1007/s00170-014-6031-0
40. APDL (2017) ANSYS Mechanical. "Release 14.0, ANSYS".
41. Thompson MK, & Thompson JM (2017) ANSYS mechanical APDL for finite element analysis. Butterworth-Heinemann.
42. Carlone P, Palazzo GS (2013) Influence of process parameters on microstructure and mechanical properties in AA2024-T3 friction stir welding. Metallography, Microstructure, and Analysis 2(4):213–222. https://doi.org/10.1007/s13632-013-0078-4
43. Handbook M. (1998) MIL-HDBK-5H metallic materials and elements for aerospace vehicle structures,1st ed. US :US Department of Defense. https://idoc.pub/documents/mil-hdbk-5hpdf-pqn8mdwowp41
44. Barron RF, & Barron BR (2011) Design for thermal stresses. John Wiley & Sons10.1002/9781118093184.app3
45. Handbook M. (1990) Vol. 2-Properties and Selection Nonferrous Alloys and Special-Purpose Mater. ASM Inter, Ohio10.31399/asm.hb.v02.9781627081627
46. Dadi SSO, Patel C, & Naidu BA (2020) Effect of friction-stir welding parameters on the welding temperature. Materials Today: Proceedings. https://doi.org/10.1016/j.matpr.2020.10.364
47. Lipski A, Mroziński S (2012) The effects of temperature on the strength properties of aluminium alloy 2024-T3. acta mechanica et automatica 6:62-66. http://yadda.icm.edu.pl/baztech/element/bwmeta1.element.baztech-article-BPB2-0068-0033
48. Aziz SB, Dewan MW, Huggett DJ, Wahab MA, Okeil AM, Liao TW (2018) A fully coupled thermomechanical model of friction stir welding (FSW) and numerical studies on process parameters of lightweight aluminum alloy joints. Acta Metallurgica Sinica (English letters) 31(1):1–18. https://doi.org/10.1007/s40195-017-0658-4
49. Jain R, Pal SK, Singh SB (2018) Finite element simulation of pin shape influence on material flow, forces in friction stir welding. Int J Adv Manuf Technol 94(5):1781–1797. https://doi.org/10.1007/s00170-017-0215-3
50. Riahi M, Nazari H (2011) Analysis of transient temperature and residual thermal stresses in friction stir welding of aluminum alloy 6061-T6 via numerical simulation. Int J Adv Manuf Technol 55(1-4):143–152. https://doi.org/10.1007/s00170-010-3038-z
51. Hodowany J, Ravichandran G, Rosakis AJ, Rosakis P (2000) Partition of plastic work into heat and stored energy in metals. Exp Mech 40(2):113–123. https://doi.org/10.1007/BF02325036
52. Peel MJ, Steuwer A, Withers PJ, Dickerson T, Shi Q, Shercliff H (2006) Dissimilar friction stir welds in AA5083-AA6082. Part I: process parameter effects on thermal history and weld properties. Metall Mater Trans A 37(7):2183–2193. https://doi.org/10.1007/BF02586138
53. Chen G, Shi Q, Feng Z (2015) On the Material Behavior at Tool/Workpiece Interface During Friction Stir Welding: A CFD Based Numerical Study in Friction Stir Welding and Processing VIII. Springer 251-258. https://doi.org/10.1007/978-3-319-48173-9_27
54. Liu X, Yu Y, Yang S, & Liu H (2020) A modified analytical heat source model for numerical simulation of temperature field in friction stir welding. Advances in Materials Science and Engineering 2020. https://doi.org/10.1155/2020/4639382

55. Yau YH, Hussain A, Lalwani RK, Chan HK, Hakimi N (2013) Temperature distribution study during the friction stir welding process of Al2024-T3 aluminum alloy. Int J Miner Metall Mater 20(8): 779–787. https://doi.org/10.1007/s12613-013-0796-2
56. Kalemba I, Hamilton C, Dymek S (2014) Natural aging in friction stir welded 7136-T76 aluminum alloy. Mater Des 60:295–301. https://doi.org/10.1016/j.matdes.2014.04.009
57. Elmetwally HT, SaadAllah HN, Abd-Elhady MS, Abdel-Magied RK (2020) Optimum combination of rotational and welding speeds for welding of Al/Cu-butt joint by friction stir welding. Int J Adv Manuf Technol 110(1):163–175. https://doi.org/10.1007/s00170-020-05815-8
58. Bastier A, Maitournam MH, Dang Van K, Roger F (2006) Steady state thermomechanical modelling of friction stir welding. Sci Technol Weld Join 11(3):278-288 https://doi.org/10.1179/174329306X102093
59. Murariu A, Veljić DM, Barjaktarević DR, Rakin MP, Radović NA, Sedmak AS, Đoković JM (2016) Influence of material velocity on heat generation during linear welding stage of friction stir welding. Therm Sci 20(5):1693-1701 10.2298/TSCI150904217M
60. Reynolds AP, Lockwood WD, & Seidel TU (2000) Processing-property correlation in friction stir welds. In Materials science forum Trans Tech Publications Ltd 331:1719-1724 10.4028/www.scientific.net/MSF.331-337.1719

Publisher's note Springer Nature remains neutral with regard to jurisdictional claims in published maps and institutional affiliations.